Pergamon

Int. J. Mech. Sci. Vol. 39, No. 6, pp. 683–695, 1997

0020-7403/97 $17.00 + 0.00

PII: S0020-7403(96)00067-7

BUBBLE GROWTH AND INK EJECTION PROCESS OF A THERMAL INK JET PRINTHEAD

PING-HEI CHEN, WEN-CHENG CHEN and S.-H. CHANG

Department of Mechanical Engineering, National Taiwan University, No. 1, Sec. 4, Roosevelt Rd, Taipei 10764, Taiwan, R.O.C.

(*Received* 20 *December* 1995; *in revised form* 23 *April* 1996)

Abstract—The present study investigated bubble growth and the ink ejection process of a thermal ink jet (TIJ) printhead with a thin-film heater on the bottom-wall of the ink nozzle. Numerical predictions are presented for bubble volume, temperature, and pressure, and ink jet ejection length under various heating conditions. An inexpensive optical system was set up to visualize the transient ink ejection process. Experimental results to show the effect of the heating pulse conditions on the ejected droplet volume and ejected ink length are also presented. The experimental and numerical results agree well on both the ejected ink length for shorter time history ($< 6\ \mu s$) and the threshold operating voltage for the ink ejection. Copyright © 1997 Elsevier Science Ltd.

Keywords: ink jet printhead, flow visualization, fluid mechanics.

NOTATION

- A inertial factor defined in Eqn (11) (m^{-1})
- B frictional factor defined in Eqn (12) (m^{-3})
- c specific heat ($J\,kg^{-1}\,K^{-1}$)
- E operating voltage of heating pulse (V)
- h_{fg} heat of vaporization ($J\,kg^{-1}$)
- K gas constant ($J\,mol^{-1}\,K^{-1}$)
- k thermal conductivity ($W\,m^{-1}\,K^{-1}$)
- L ejected ink length (μm)
- P pressure (Pa)
- P_{atm} atmospheric pressure (Pa)
- P_s saturated vapor pressure (Pa)
- R resistance (Ω)
- R_{all} total resistance of resistor and electrodes (Ω)
- r, z cylindrical coordinates for the ink flow in the nozzle (m)
- T temperature (°C)
- T_{amb} ambient temperature (°C)
- T_{bp} temperature at the boiling point of ink (°C)
- t time (s)
- t_b onset time of homogeneous nucleation (or bubble growth) (s)
- u_{ave} averaged axial ink velocity over the cross-section of the nozzle (ms^{-1})
- V volume (m^3)
- V_{max} maximum bubble volume (m^3)
- W width of heating pulse (μs)
- w molecular weight ($kg\,mol^{-1}$)
- x vertical coordinate for the heat conduction in the printhead (m)
- z_{tip} z-coordinate value of the tip of ejected ink (m)
- λ empirical constant in Eqn (5)
- μ dynamic viscosity ($kg\,m^{-1}\,s^{-1}$)
- ρ density ($kg\,m^{-3}$)
- τ time constant of vapor bubble pressure decay in Eqn (5) (s)

Subscripts

- $(\ )_d$ droplet
- $(\ )_e$ exit of nozzle
- $(\ )_f$ ejected ink
- $(\ )_h$ thin-film resistor
- $(\ )_{hi}$ heater–ink interface
- $(\ )_i$ bubble–ink interface
- $(\ )_t$ at the threshold condition for homogeneous nucleation
- $(\ )_v$ vapor bubble

1. INTRODUCTION

A typical thermal ink jet (TIJ) printhead is composed of a thin-film heater driven by a power-input controller and an ink nozzle for storing the ink. The operation cycle of the TIJ printhead can be simply divided into three sequential steps, as shown in Fig. 1. In the first step, the thin film resistor of the heater is rapidly heated by an electrical pulse of several microseconds. Such a pulse can generate power densities in the order of several megawatts per square meter. Consequently, a sharp temperature rise in the ink results from the high heat flux coming from the thin-film resistor, as shown in Fig. 1(a). The ink temperature near the heater–ink interface quickly reaches the threshold temperature, T_t, above which homogeneous nucleation takes place in the ink. Once the homogeneous nucleation occurs, a vapor bubble with high pressure (> 10 atm) is then formed in the ink. The second step of the operation cycle starts from the moment that a vapor bubble is formed. As the vapor bubble grows, it causes ink flow in the nozzle and ink ejection at the exit, as illustrated in Fig. 1(b). Due to the fast growth of the vapor bubble and the evaporation of ink, the temperature and pressure in the vapor bubble quickly decrease. At the end of the second step, a droplet then breaks away from the ejected ink, as shown in Fig. 1(c). The break-off of the droplet from the ejected ink occurs nearly simultaneously with the collapse of the bubble. In the third step, the nozzle is refilled with ink after the collapse of the bubble, as shown in Fig. 1(d).

The characteristics of the ejected ink jet are significantly affected by ink properties, heat conduction in the heater, heating pulse conditions, and induced ink motion in the nozzle. To obtain good print quality, the aforementioned characteristics in the micro-scale thin-film structure should be carefully studied.

In the last 10 years, several articles have reported both numerical and experimental results which are related to the bubble jet printhead. There are two kinds of thermal bubble ink jet printheads on the market: one has the heater on the ink nozzle side wall (side shooters), and the other has the heater on the nozzle bottom wall (front shooters). The prior studies focused on fluid dynamics and bubble growth in side-wall heater printheads.

For the side-shooter printheads, a series of studies have been conducted by researchers at Canon Inc. Asai *et al.* [1] used a one-dimensional model to perform numerical calculations to predict the bubble growth and collapse, as well as ink flow motion in the nozzle. To determine the required heating conditions for bubble jet operation, Asai *et al.* [2] conducted experiments in which they

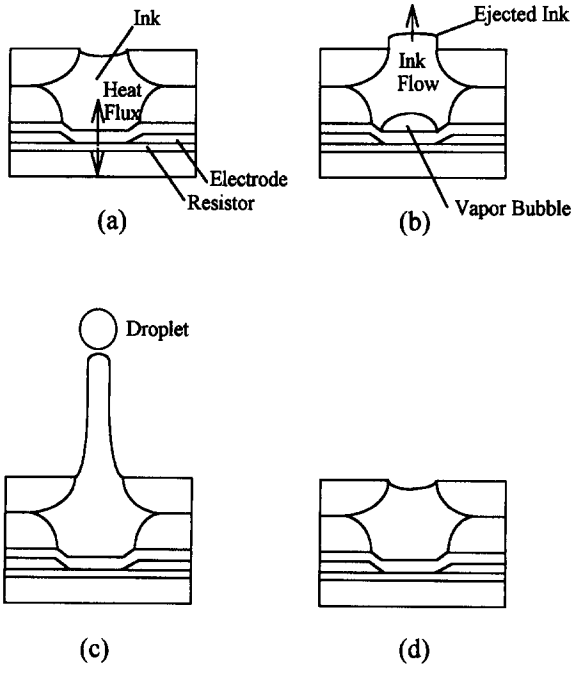

Fig. 1. Schematic graphs for the ink droplet generation cycle: (a) heating of ink; (b, c) bubble growth and ink ejection; (d) ink refill.

observed boiling types for different printheads under various heat pulse conditions. Their measured results showed that only homogeneous nucleation could be capable to propel an ink jet in the typical printhead. To improve the understanding of the boiling process, Asai [3] presented a theoretical model to predict the incipient boiling time. A refined model was also proposed by Asai [4] to predict the bubble behavior after the occurrence of homogeneous nucleation. In addition, Asai [5] employed a finite-difference method to solve the three-dimensional Navier–Stokes equations to predict the fluid motion of the ink jet. For a piezoelectric ink jet printhead, Fromm [6] employed the finite-difference method to analyze the development of a laminar ink jet ejected from the nozzle. Allen *et al.* [7] modeled vapor bubble generation and fluid motion of an ink jet for a front-shooter printhead. However, few experimental studies have been conducted to investigate ink ejection for this type of printhead.

The aim of the present study is to employ both numerical and experimental methods to study bubble growth and the ink ejection process for TIJ bottom-wall heater printheads. Numerical predictions are conducted to examine the effects of heating pulse width and operating voltage on both bubble growth and ink ejection. An inexpensive optical system was set up to visualize the ink ejection process and to measure the ejected droplet volume. Comparison between numerical and experimental results is presented.

2. THEORETICAL MODEL AND NUMERICAL METHOD

Figure 2 shows a schematic view of the examined printhead. Note that the heater nozzle has a circular cross-section with radius of 32.5 μm but the resistor has a rectangular cross-section of 65 μm $\times$ 65 μm. The physical properties and the thickness for each layer in the thin-film structure are listed in Table 1. In this study, the water-based ink is made of water, 1,2-butanediol, and 2-pyrrolidinone and has a dynamic viscosity of 1.28 cp. The weight fraction of water in the ink is 86.5%.

2.1. *Heat conduction in the printhead*

After the heating pulse is applied, the unsteady heat conduction problem for in the printhead can be modeled with the following one-dimensional heat diffusion equation [1]:

$$\frac{\partial}{\partial x}\left(k\frac{\partial T}{\partial x}\right)+\left(\frac{E}{R_{\mathrm{all}}}\right)^2\left(\frac{R_{\mathrm{h}}}{V_{\mathrm{h}}}\right)=\rho c\frac{\partial T}{\partial t} \tag{1}$$

where k, ρ, and c denote the thermal conductivity, density and specific heat of the material, respectively, at the vertical location x. In Eqn (1), E is the operating voltage, V_{h} is the resistor volume, R_{h} denotes the electrical resistance of the resistor, and R_{all} denotes the total electrical resistance of the resistor with extended electrodes. In this study, the values of R_{h} and R_{all} are 35 and 46 Ω, respectively, and are assumed to be constant in the range of operation. The above unsteady heat conduction problem is subject to the following initial and boundary conditions:

$$\begin{aligned} &T = T_{\mathrm{amb}} \quad \text{at } t = 0 \text{ for } 0 \leqslant x \leqslant x_{\mathrm{e}} \\ &T = T_{\mathrm{amb}} \quad \text{at } x = 0 \text{ and } x = x_{\mathrm{e}} \text{ for } t > 0. \end{aligned} \tag{2}$$

An implicit finite-difference numerical scheme was employed to solve Eqns (1) and (2). Since the thermal conductivity of the ink is relatively low, the sharp thermal gradient is expected in the heater–ink interface region. Thus, a non-uniform grid was used. The numerical experiments were carried out to find the time increment and grid resolution sufficient for convergence at $E = 18$ V. The time increment of 0.01 μs and 341 grids were found and used throughout the present simulation. Table 1 also lists the number of divisions in the computation for each layer of the printhead.

With the high heat flux conducted into the ink, an empirical correlation [8] was used to predict the threshold temperature T_{t}, given by

$$T_{\mathrm{t}}(^{\circ}\mathrm{C}) = 230^{\circ}\mathrm{C} + 1.6\cdot 10^{-7}\cdot\left(\frac{\partial T}{\partial x}\right)_{\mathrm{hi}} \tag{3}$$

where $(\partial T/\partial x)_{\mathrm{hi}}$ denotes the temperature gradient in ink at the heater–ink interface. Once the temperature at the ink–heater interface is greater than T_{t}, homogeneous nucleation following the film boiling immediately takes place. The induced vapor bubble quickly covers the bottom surface of

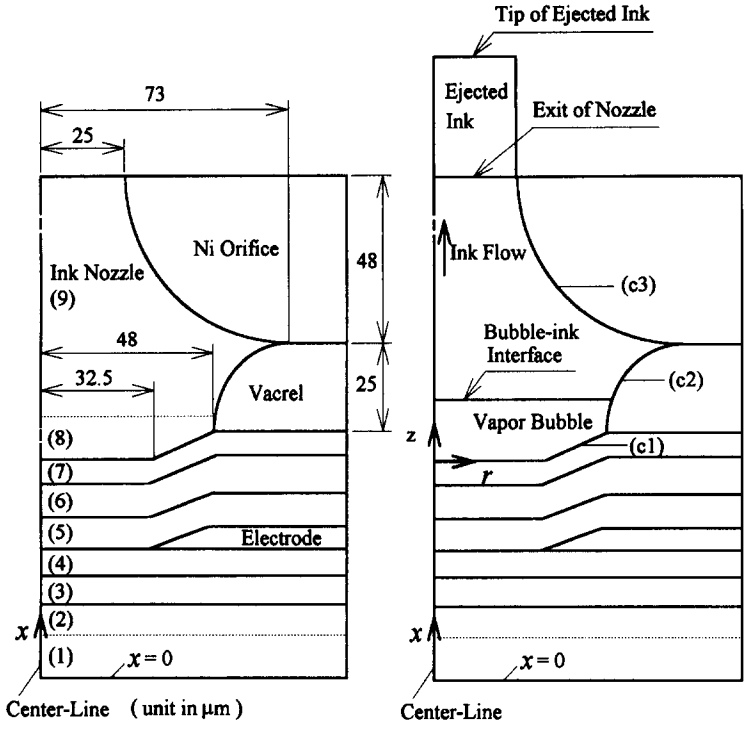

Fig. 2. Geometry of the examined printhead with numerical simulation coordinates: (a) the first step (heating of ink); (b) the second step (ink ejection).

Table 1. Data used for each layer of the printhead in the numerical simulation

Number in Fig. 2	Material	ρ (kg m^{-3})	c(J kg^{-1} K^{-1})	k(W m^{-1} K^{-1})	Thickness (μm)	Number of divisions for numerical simulation
1	Si	2.34×10^3	7.6×10^2	168	500	100
2	Si	2.34×10^3	7.6×10^2	168	25	20
3	SiO_2	2.07×10^3	8.4×10^2	1.4	1.7	20
4	HfB_2	2.77×10^3	1.0×10^3	10.9	0.1	20
5	Si_3N_4	3.20×10^3	7.9×10^2	1.67	0.5	20
6	SiC	3.25×10^3	6.72×10^2	33.5	0.5	20
7	Ta	1.66×10^4	1.5×10^2	57	0.25	20
8	Ink	1.02×10^3	4.2×10^3	0.61	10	100
9	Ink	1.02×10^3	4.2×10^3	0.61	63.5	20

the nozzle and the height of vapor bubble is assumed to be uniform across the cross-section of nozzle. The operation cycle now progresses into the second step.

2.2. *Ink flow in the nozzle*

The ink in the nozzle is assumed to be incompressible and its surface tension is neglected in this case. We also assume the vapor to be an ideal gas with the uniform vapor temperature and pressure.

According to Refs [1, 4, 5], the vapor pressure in the bubble initially ranges from 1 to 10 MPa, and then, within a few microseconds, decreases to the saturated water vapor pressure at ambient temperature. To predict the vapor pressure, Asai [4] classified the process of bubble growth into two stages. In the early stage, the Clausius–Clapeyron equation is adequate to describe the pressure in the vapor bubble, P_v, for the water-based ink, given by

$$P_v = P_{atm} \exp\left[\frac{wh_{fg}}{K}\left(\frac{1}{273 + T_{bp}} - \frac{1}{273 + T_v}\right)\right]. \tag{4}$$

Here, K is the gas constant, w denotes the molecular weight of the water vapor in the bubble, and h_{fg} and T_{bp} denote the heat of vaporization and boiling point temperature of water at 1 atm, respectively. Note that Eqn (4) is only valid when the vapor bubble height is thin and the ink flow velocity is small.

A first-order exponential decay formula was suggested by Asai [4] to describe the sharp drop in the vapor pressure in the later stage of the bubble growth process, given as

$$P_v = (P_t(T_t) - P_s(T_{amb}))\exp\left(-\left(\frac{t - t_b}{\tau}\right)^{\lambda}\right) + P_s(T_{amb}) \tag{5}$$

where t_b denotes the onset time of homogeneous nucleation in the ink, τ is the time constant, and P_t and P_s are the values for saturated vapor pressure at T_t and T_{amb}, respectively. In Eqn (5), the λ value can range from 0.5 to 1.5 [4]. The λ value is carefully selected by matching the time histories between the measured and predicted ejected ink lengths. In this study, a λ value of 0.5 was used. Following the criterion suggested by Asai [4], Eqn (4) is not valid after the heat flux transferred from the heated ink into the bubble has reached the maximum value. At the instant of the maximum heat flux, the time constant τ can be solved by letting the obtained vapor pressure values in Eqns (4) and (5) be equal at a given λ value.

The back flow from the nozzle into the ink reservoir is assumed to be negligible. Accordingly, the growth rate of vapor bubble volume is equal to that of the volume of ink ejected out of the nozzle. Thus, the ink motion in the nozzle can be modeled as a one-dimensional hydraulic motion [9]. In the early stage of bubble growth, the ink flow motion is given by

$$\rho_f A \frac{d^2 V_f}{dt^2} + \mu_f B \frac{dV_f}{dt} = P_v - P_{atm} \tag{6}$$

where V_f denotes ink volume ejected out of the nozzle and μ_f is the dynamic viscosity of the ink. Equation (6) is subject to the initial conditions:

$$V_f(t) = 0 \quad \text{and} \quad dV_f/dt = 0 \quad \text{at } t = t_b. \tag{7}$$

In the later stage of bubble growth, the bubble vapor pressure rapidly decreases to the saturated vapor pressure at the ambient temperature in a few microseconds. Thus, the vapor pressure that serves as the driving force for the ink fluid motion can be further simplified to a pressure impulse function [4],

$$P_v \approx (P_t\tau/\lambda)\delta(t - t_b) + P_s \tag{8}$$

where $\delta(t - t_b)$ is the Dirac delta function. Substituting Eqn (8) into Eqn (6), yields an alternative form of the governing equation for the ink fluid motion in the later stage, expressed by

$$\rho_f A \frac{d^2 V_f}{dt^2} + \mu_f B \frac{dV_f}{dt} = P_s(T_{amb}) - P_{atm} \tag{9}$$

and is subject to the initial conditions:

$$V_f(t) = 0 \quad \text{and} \quad (dV_f/dt) = (P_t\tau/\rho_f A\lambda) \quad \text{at } t = t_b^+. \tag{10}$$

A similar expression was also derived by Asai [4] to describe the ink fluid motion for a bubble generated on side wall of the nozzle.

In Eqns (6), (9) and (10), factors A and B are called the inertial factor and frictional factor, respectively, for the ink flow motion in the nozzle, and are expressed by:

$$A = \frac{r_i^2}{\pi r_e^2} \int_{z_i(t-t_b)}^{z_e} r^{-2}\,dz \tag{11}$$

$$B = \frac{8}{\pi} \int_{z_i(t-t_b)}^{z_e} r^{-4}\,dz \tag{12}$$

where z_i and z_e denote the locations of the bubble–ink interface and nozzle exit, respectively, and r_i and r_e are the radii of the nozzle cross-section at the bubble–ink interface and at the nozzle exit, respectively. The nozzle profile is shown in Fig. 2(b).

2.3. *Energy equation in the ink fluid flow*

By considering the area change of the divergent-convergent nozzle, the one-dimensional energy equation for the ink flow is expressed by

$$\rho_f c_f \left[\frac{\partial T_f}{\partial t} + u_{ave}\frac{\partial T_f}{\partial z}\right] = k_f \frac{1}{\pi r^2}\frac{\partial}{\partial z}\left(\pi r^2 \frac{\partial T_f}{\partial z}\right) = k_f \frac{\partial^2 T_f}{\partial z^2} + k_f \frac{2}{r}\frac{dr}{dz}\frac{\partial T_f}{\partial z} \tag{13}$$

where T_f is the ink temperature in the nozzle, c_f and k_f are the specific heat and thermal conductivity of the ink, respectively, and $u_{ave} = 1/\pi r^2\,(dV_f/dt)$ denotes the average axial ink velocity over the cross-section of the nozzle at the location z.

Equation (13) is subject to the following initial and boundary conditions:

$$\begin{aligned} T_f &= T_f(z) && \text{at } t = t_b^+ \text{ for } z_i \leqslant z \leqslant z_{tip} \\ T_f &= T_{amb} && \text{at } z = z_{tip} \text{ for } t > t_b^+ \\ h_{fg}\rho_v(dV_f/dt) &= \pi r_i^2 k_f (\partial T_f/\partial z)_i && \text{at } z = z_i \text{ for } t > t_b^+ \end{aligned} \tag{14}$$

where $(\partial T_f/\partial z)_i$ is the temperature gradient in the ink at the liquid–vapor interface.

Equations (13) and (14) were solved by an implicit finite-difference method, using a numerical scheme [10] to convert the moving grid system in the physical domain into a fixed grid system in the computational domain.

3. EXPERIMENTAL APPARATUS AND PROCEDURE

A schematic view of the optical measuring system is shown in Fig. 3. This system was set up to observe the droplet ejection process and to measure the volume of ink droplets. The measuring system consists of a controller with a liquid crystal display (LCD), a pulse generator with a power amplifier, a light emitting diode (LED) stroboscope, a microscope, a charge-coupled device (CCD) camera, a precision three-axis table, an electric balance, and a 486 IBM-compatible personal computer. The printhead was installed on the top of the three-axis table and the nozzle exit is

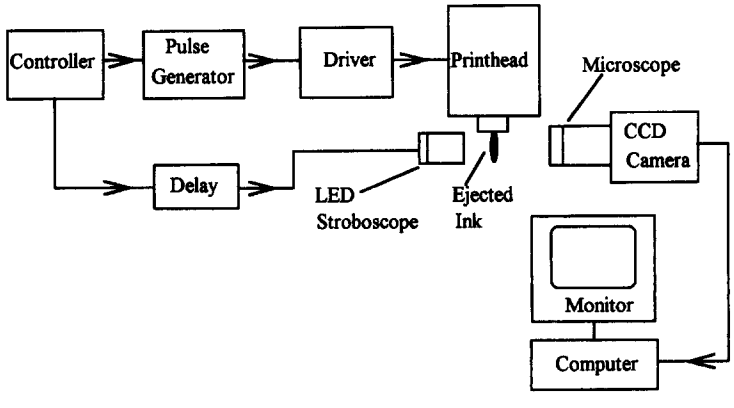

Fig. 3. Schematic view of the optical system for ink ejection visualization.

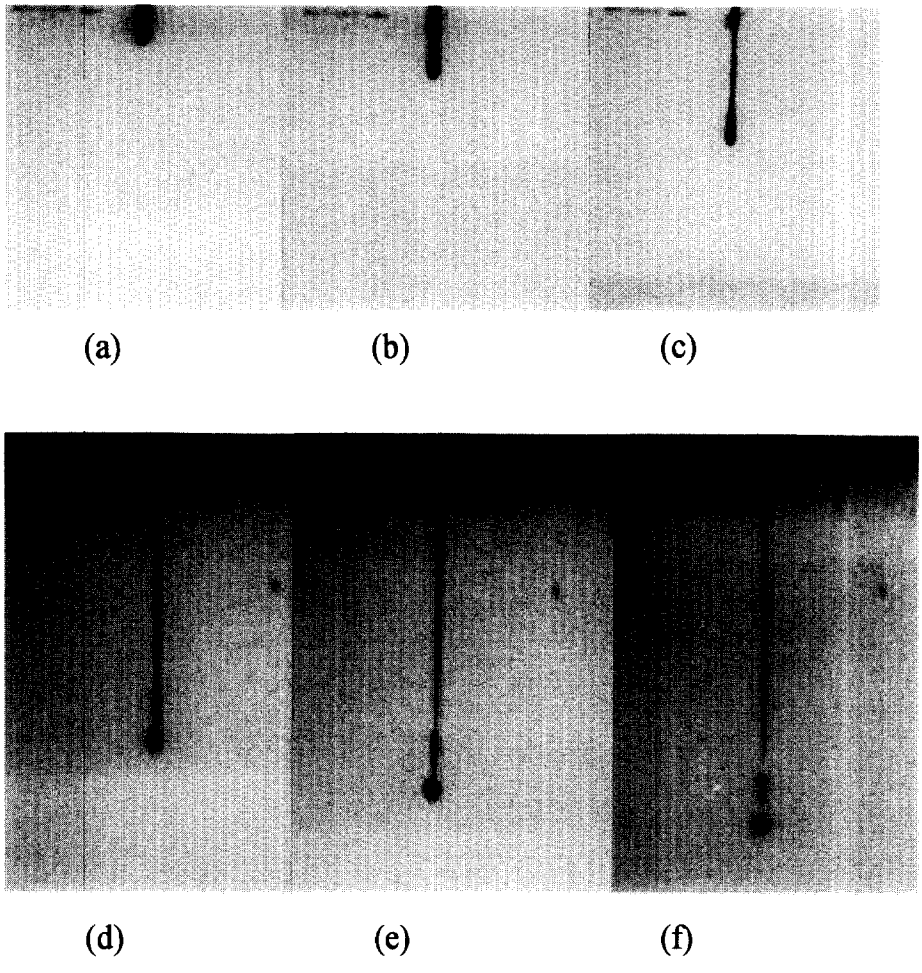

Fig. 4. Temporal evolution of the ink ejection at $E = 17$ volts and $W = 3$ μs: (a) $t = 6$ μs, $L = 61$ μm; (b) $t = 10$ μs, $L = 132$ μm; (c) $t = 20$ μs, $L = 295$ μm; (d) $t = 50$ μs, $L = 737$ μm; (e) $t = 55$ μs, $L = 832$ μm; (f) $t = 60$ μs, $L = 901$ μm.

oriented toward gravity. The uncertainty in measuring the distance moved by the precision table is $\pm$ 2.5 μm.

The function of the controller is to control the operating voltage, frequency, number of pulses, and pulse width of the electrical heating pulse. All of these data can be read from the LCD panel of the controller. After the resistor was heated by the electrical heating pulse, the droplet ejection process was observed through a microscope with $\times$ 10 magnification using a synchronized stroboscope light emitted from the LED. The stroboscope light elapsed emission time was controlled by a delay unit which was triggered by the controller. Thus, the image of the ejected ink was captured by the CCD camera with the same elapsed time after the heating pulse was applied to the resistor. The image captured by the CCD camera was digitized by a frame grabber, displayed on the monitor screen, and was then stored in a file.

The determination of the length of ejected ink was simply accomplished by measuring the ejection length on the monitor screen. The average droplet volume was calculated by dividing the total volume of the ejected droplets by the total number of heating pulse. The total volume of the ejected droplets was calculated by the total measured mass of the ejected droplets divided by the ink density. In a typical run, 1–2 million ejected droplets, with a mass of 120–240 mg, are collected for mass measurement. Since the number of heating pulses can be accurately counted, the uncertainty in the average volume measurement is attributed to the error in mass measurement. The electric balance used in the present study has a resolution of 1 mg. Accordingly, based on a 95% confidence level, the uncertainty in droplet volume measurement is around $\pm$ 1.73%.

In the experimental measurements, the frequency of the heating pulse was fixed at 1 kH, and the operating voltage and pulse width were varied in a range from 15 to 21 V and 3 to 8 μs, respectively.

4. RESULTS AND DISCUSSION

Figure 4 shows the measured ink ejection process at $E = 17$ V and $W = 3$ μs. In Fig. 4(a), the ejected axisymmetric ink jet has a uniform diameter of $t = 6$ μs. As time progresses, the shape of the ink jet gradually changes from the column shape at $t = 6$ μs to an eyedrop-like shape at $t = 20$ μs [Fig. 4(c)] because the ink jet has a faster velocity at the tip than that at the nozzle exit. This is probably due to the fact that less friction is encountered by the ink flow in air than in the solid nozzle. In Fig. 4(d), the tip of the ink jet is 737 μm away from the nozzle exit but the round droplet is not formed yet at $t = 50$ μs. At $t = 55$ μs, a round droplet just flies away from the ejected ink jet, as shown in Fig. 4(e). At $t = 60$ μs, Fig. 4(f) shows the appearance of a small satellite droplet. For the

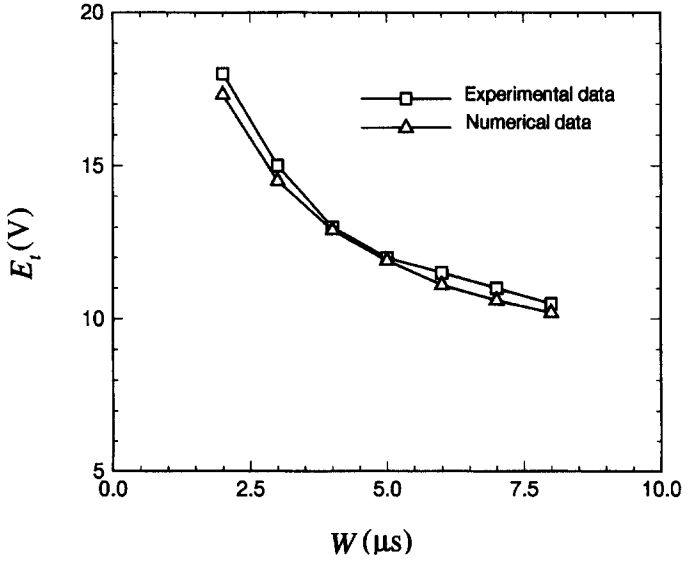

Fig. 5. Comparison between numerical and experimental results at threshold operating voltages for ink ejection at various W values.

best printing quality, the ink should reach the paper after the main droplet is formed, but before the appearance of any satellite droplets.

A comparison between the predicted and measured threshold operation voltages for ink ejection at a range of heating pulse width is presented in Fig. 5. For the numerical results, the threshold voltage was taken to be the value at which the heat generated by the resistor was enough to heat up the ink just beyond the threshold temperature, T_t, at the end of heating pulse. An empirical correlation between E_t and W was obtained by a curve fit using the least-squares method, given by

$$E_t = 22.94\, W^{-0.39}. \tag{15}$$

The threshold operating voltage E_t decreases with an increase in the heating pulse width. This is due to the larger operating voltage required for a smaller heating pulse width in order to generate sufficient heat for ink bubble generation.

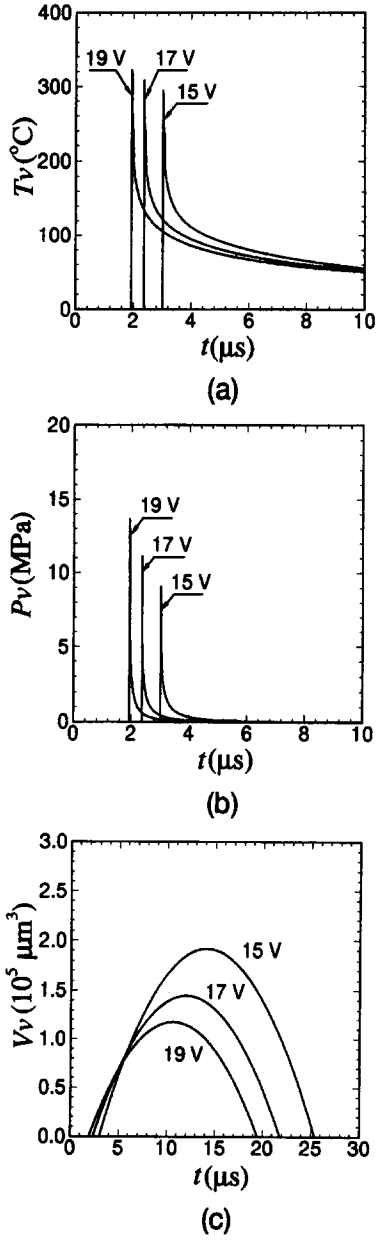

Fig. 6. Predicted time histories of bubble variables at various operating voltages with $W = 3$ μs: (a) temperature; (b) pressure; (c) volume.

At various E values and $W = 3$ μs, the predicted time histories of bubble temperature, pressure and volume are illustrated in Fig. 6(a–c). In Fig. 6(a), the threshold temperature is larger for the case with a greater operating voltage. The threshold temperatures are all above the boiling temperature (100°C), but less than the critical temperature (374°C) for water at 1 atm. In Fig. 6(b), the saturated vapor pressure at T_t is much greater than atmospheric pressure and its value is significantly affected by the operating voltage. The vapor pressure falls from several MPa to a few kPa in a few microseconds as the vapor bubble grows. Although the initial vapor pressure increases with operating voltage for a fixed W value, Fig. 6(c) shows that the onset time of vapor bubble formation, the maximum bubble volume, and the lifetime of a bubble all decrease with the rise in the operating voltage. The reason is explained as follows. At a higher operating voltage, the incipience of homogeneous nucleation occurs earlier, thus less heat energy is transferred into the ink from the heater before the incipience of homogeneous nucleation. Accordingly, there is less heat energy stored in the ink which can be used later to vaporize the liquid ink for supporting the vapor bubble growth.

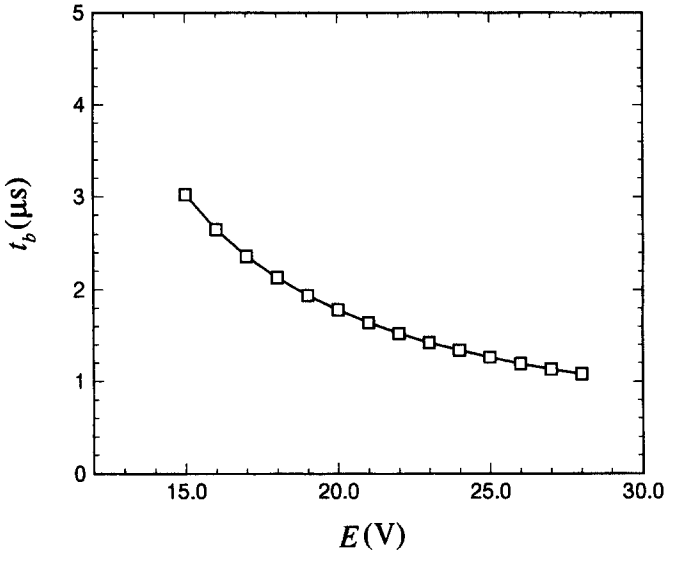

Fig. 7. Predicted onset time of bubble growth versus operating voltage at $W = 3$ μs.

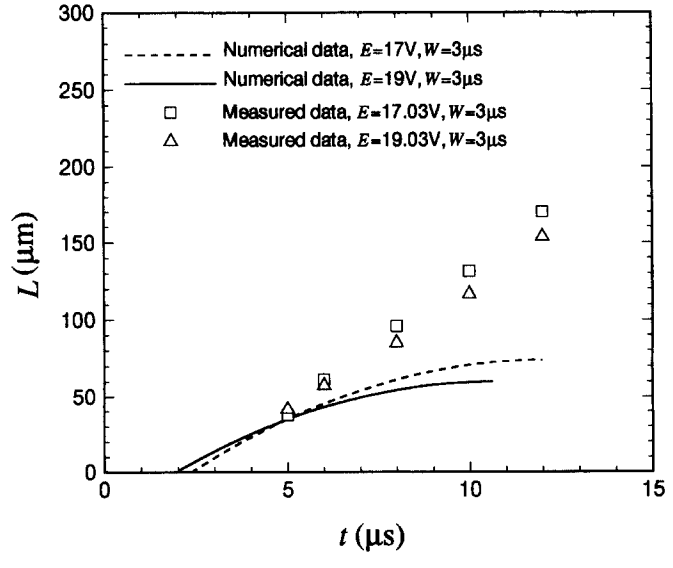

Fig. 8. Comparison between the numerical and measured ejected ink lengths.

Predicted results are presented in Fig. 7 to show the effect of operating voltage on the onset time of bubble formation for $W = 3$ μs. From the predicted results, the onset time of bubble formation is approximately proportional to $E^{-1.6}$. Note that the operating pulse width should be controlled to a value slightly longer than t_b to avoid heating the resistor to a temperature higher than the allowable material temperature.

Figure 8 shows a comparison between the numerical data and measured results for the ejected ink length. In the numerical data, the ejected ink length was determined by dividing the ejected ink volume by the cross-sectional area at the nozzle exit. That is, the ink jet is assumed to have a cylindrical shape. The difference between numerical and experimental results gradually becomes greater as time progresses. This is probably due to the shape change in the ink jet resulting from the axial velocity variation in the ejected ink. In addition, increasing the operating voltage results in a shorter ejected ink length at the same time instant t. This finding is also confirmed by the predicted results of the vapor bubble volume versus the operating voltage, as showing in Fig. 6.

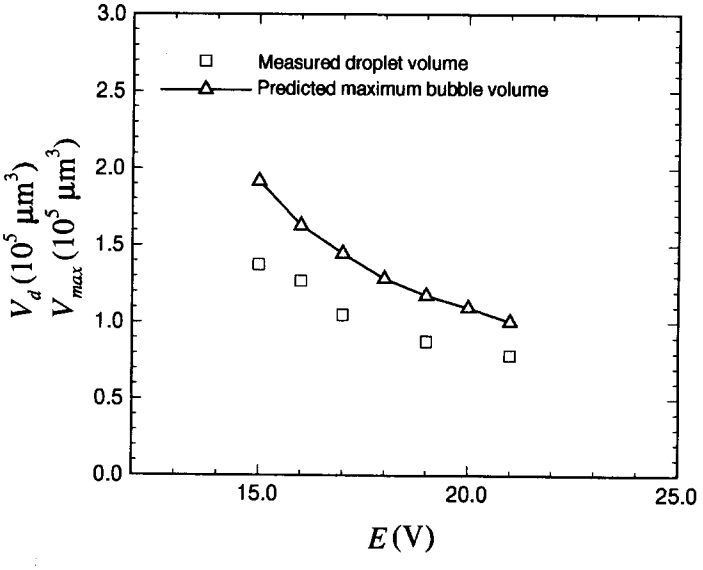

Fig. 9. The measured droplet volume and the predicted maximum bubble volume versus operating voltage at $W = 3$ μs.

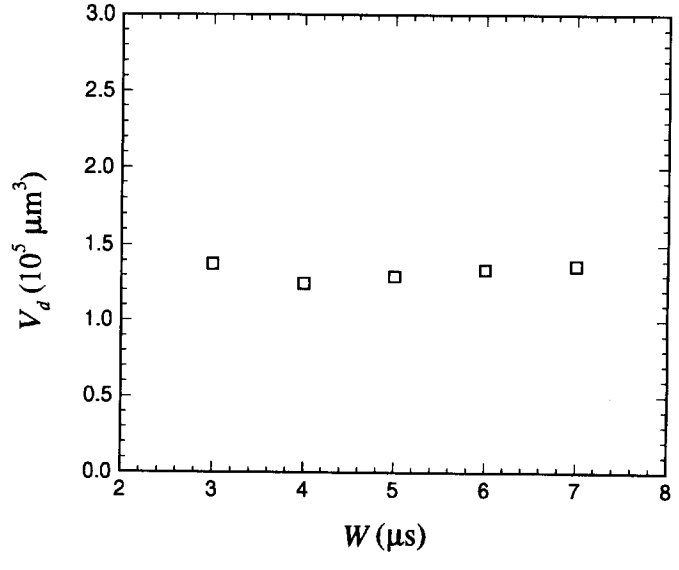

Fig. 10. Measured droplet volumes at various heating pulse conditions at $E = 15$ V.

The predicted volume of the ejected droplet hitting the printing paper could be overestimated if the maximum bubble volume is considered to be the ejected droplet volume. Figure 4(e–f) clearly shows that not all the ink expelled from the nozzle forms a droplet for printing purposes. Figure 9 presents a comparison between the maximum bubble and ejected droplet volumes at various operating voltages for $W = 3$ μs. Note that the measured volume includes both main and satellite droplets. About 71–78% of the ejected ink jet (equivalent to the maximum bubble volume) becomes the departed droplet. As observed in Fig. 9, the ejected droplet volume decreases as the operating voltage increases at a fixed W value.

Figure 10 shows the effect of heating pulse width on the measured droplet volume at $E = 15$ V. It can be seen that the droplet volume is slightly affected by the variation of heating pulse width. This is because the water vapor serves as the thermal insulator as the vapor bubble is generated between the heater and the water ink. Thus, the heat generated by the heater is no longer transferred to the ink after the bubble is formed.

5. CONCLUSIONS

A one-dimensional model was used to describe the unsteady conduction problem, bubble growth, and ink motion of the test front-shooter TIJ printhead. In addition, an inexpensive optical system was set up to measure the ejected ink length and ejected droplet volume. Conclusions can be drawn from the presented numerical and experimental results as follows. The threshold operating voltage for ink ejection decreases with the heat pulse width. Based on the measured results, the correlation between the threshold operating voltage and pulse width is expressed as $E_t = 22.94\, W^{-0.39}$ for $2 \leqslant W \leqslant 8$ μs. Increasing the operating voltage results in earlier bubble nucleation and smaller maximum bubble volume for a fixed W value. The measured ejected ink lengths agree well with the predicted data for $t < 6$ μs. In addition, the measured ejected droplet volume is less than the predicted maximum bubble volume because only a portion of the ink jet ejected from the nozzle forms the ejected droplet for printing. In the range of operating voltages studied, increasing the operating voltage causes a smaller ejected droplet volume at a fixed W value. Therefore, the ejected droplet volume is only slightly affected by the variation of heating pulse if the operating voltage is kept at a constant value.

Acknowledgements—The authors like to thank Dr Y.-L. Lan, of Opto-Electronics & System Labs of ITRI in Taiwan, R.O.C., for his help to provide the ink properties, geometrical data of printhead, and test printhead.

REFERENCES

1. Asai, A., Hara, T. and Endo, I., One-dimensional model of bubble growth and liquid flow in bubble jet printers. *Japan Journal of Applied Physics*, 1987, **26**, 1794–1801.
2. Asai, A., Hirasawa, S. and Endo, I., Bubble generation mechanism in the bubble jet recording process. *Journal of Imaging Technology*, 1988, **14**, 120–124.
3. Asai, A., Application of the nucleation theory to the design of bubble jet printers. *Japan Journal of Applied Physics*, 1989, **28**, 909–915.
4. Asai, A., Bubble dynamics in boiling under high heat flux pulse heating. *ASME Journal of Heat Transfer*, 1991, **113**, 973–979.
5. Asai, A., Three-dimensional calculation of bubble growth and drop ejection in a bubble jet printer. *ASME Journal of Fluids Engineering*, 1992, **114**, 638–641.
6. Fromm, J. E., Numerical calculation of the fluid dynamics of drop-on-demand jets. *IBM Journal of Research and Development*, 1984, **28**, 322–333.
7. Allen, R. R., Meyer, J. D. and Knight, W. R., Thermodynamics and hydrodynamics of thermal ink jets. *HEWLETT-PACKARD Journal*, 1985, **36**, 21–27.
8. Runge, W., Nucleation in thermal ink-jet printers. In *IS&T's 8th International Congress on Advances in Non-Impact Printing Technology*. The Society of IS&T, Virginia, 1992, p. 299–302.
9. Beasley, J. D., Model for fluid ejection and refill in an impulse drive jet. *Photographic Science Engineering*, 1977, **21**, 78–82.
10. Kang, I. S. and Leal, L. G., Numerical solution of axisymmetric, unsteady free-boundary problems at finite Reynolds number—1. Finite-difference scheme and its application to the deformation of a bubble in a uniaxial straining flow. *Physics of Fluids*, 1987, **30**, 1929–1940.